



Selective catalytic oxidation of ammonia to nitrogen over CuO-CeO₂ mixed oxides prepared by surfactant-templated method

Zhong Wang, Zhenping Qu*, Xie Quan, Zhuo Li, Hui Wang, Rui Fan

Key Laboratory of Industrial Ecology and Environmental Engineering (MOE), School of Environmental Sciences and Technology, Dalian University of Technology, Linggong Road 2, Dalian, 116024, China

ARTICLE INFO

Article history:

Received 23 September 2012

Received in revised form

20 December 2012

Accepted 8 January 2013

Available online 26 January 2013

Keywords:

Selective catalytic oxidation of ammonia

CuO-CeO₂ mixed oxides

NH₃ activation

Oxygen migration

Active species

ABSTRACT

The selective catalytic oxidation of ammonia to nitrogen (NH₃-SCO) has been studied over CuO-CeO₂ mixed oxides. The active Cu component was doped into the CeO₂ by surfactant-templated method. The finely dispersed CuO, Cu-O-Ce solid solution and bulk CuO species were detected in CuO-CeO₂ mixed oxides. When the Cu loading was 10 wt% and the calcination temperature was 500 °C, CuO-CeO₂ catalyst exhibited the highest molar ratio of the finely dispersed CuO species and the smallest CeO₂ particles in size, and simultaneously possessed the highest level of activity. The finely dispersed CuO species was the main adsorbed sites of NH₃ molecules, and the NH_{3(ad)} could be further activated and transformed into NH_x species by ceria under the roles of quick change of chemical state in near-surface region and the strong electron state interaction in CuO-CeO₂ catalysts. The synergetic interaction between the two components played an important role in NH₃ activation and oxidation. In addition, the activated intermediates (NH_x) could also react with lattice oxygen provided by Cu-O-Ce solid solution to form N₂, N₂O and H₂O, which was confirmed by XPS, EPR and NH₃-TPR analysis. Moreover, gas oxygen could refill the oxygen vacancies to replenish the lattice oxygen consumed by NH_x species. The Cu-O-Ce solid solution promoted the activation of gas oxygen as well as the formation and migration of lattice oxygen in NH₃-SCO reaction, and the formed rapid reduction-oxidation cycle was essential for the higher activity of NH₃ oxidation.

© 2013 Elsevier B.V. All rights reserved.

1. Introduction

The removal of ammonia from industrial waste streams and agricultural sources is becoming an increasing important issue because of environmental concerns. Selective catalytic oxidation (SCO) of ammonia with O₂ to nitrogen is a potentially ideal technology nowadays to abate NH₃ pollution and consequently it has become of increasing interest in recent years [1–4]. Noble metals such as Ag, Pt, Pd, Ru and Ir exhibited remarkably more active and long-term stability as catalysts at relatively low temperature for the ammonia oxidation, but the high cost and low N₂ selectivity limited their widespread application [2,5,6].

Due to the limited availability of noble metals, more attention has been focused to transition metals including CuO, Fe₃O₄, Co₃O₄, MnO₂, MoO₃, NiO [5,7,8]. Among them, the catalysts containing copper ion were found to be some of the most interesting system because of its higher reducibility and low price. Sazonova et al. [9] and He et al. [6] have reported that the Cu supported on TiO₂ catalyst possessed a relatively good performance for SCO of ammonia at around 300 °C. Lu et al. [7] obtained that copper alumina catalysts

showed the best NH₃ conversion at 350 °C. The 93% NH₃ conversion was achieved over the CuO/La₂O₃ (8:2, mol/mol) catalyst at 400 °C during catalytic oxidation with oxygen content of 4% [10]. As a whole, however, the conversion temperature of maximum catalytic activity of ammonia oxidation over copper-containing catalysts was still high (>300 °C). Accordingly, the development of novel and more effective copper-containing catalysts was a critical requirement for NH₃-SCO reaction. It has been known that as one of the rare earth oxides, ceria (CeO₂) exhibited high oxygen storage capacity (OSC), rich oxygen vacancies, strong interaction with metal, and the ability to shift easily between Ce³⁺ and Ce⁴⁺ [11,12]. Moreover, the catalytic activity could be significantly enhanced if other metal ions such as Cu were doped into the CeO₂, which was due to the interaction of ceria with Cu ions [13]. The CuO-CeO₂ mixed metal oxide has become an efficient catalyst for various reactions, such as the combustion of methane [14], water-gas shift (WGS) [15], preferential CO oxidation (CO-PROX) [16], NO reduction [17], methanol synthesis [18], phenol steam reforming [19], and so forth. For instance, for the CO oxidation reaction, the CuO-Ce catalysts have demonstrated specific activities far superior to the conventional copper-based catalysts and even comparable with or superior to platinum catalysts [20]. Besides, Lou et al. [21] have also considered the oxidation of ammonia over copper-cerium composite catalyst prepared by co-precipitation, but the reaction

* Corresponding author. Tel.: +86 411 8470 8083; fax: +86 411 8470 8083.

E-mail address: quzhenping@dlut.edu.cn (Z. Qu).

temperature was too high and $\sim 99.2\%$ NH_3 conversion could only be achieved at 400°C over Cu–Ce (6:4, mol/mol) catalyst. Moreover, the interaction between Cu and Ce species and catalytically active sites in ammonia oxidation was not obviously expounded.

Actually, many investigations about the roles played by ceria and copper species in CuO–CeO₂ catalysts have been extensively studied, and it was found that the active species sites for reactants as well as the roles of the Cu and CeO₂ were distinctive in different reactions. Ovesen et al. [22] have proposed either metallic Cu or Cu⁺ ions as active sites for the WGS reaction. Marino et al. [23] reported that easily reduced Cu nanoparticles, compared to bulk CuO, could easily adsorb CO, resulting in highly active and selectivity in the CO-PROX. Moreover Ce species might not be a simple spectator but play a direct role in the catalytic process [24,25]. The ceria species could hinder Cu sintering, form strong interactions at CuO–CeO₂ junctures and enhance the thermal stability [26]. In addition, many studies demonstrated that the Cu partly integrated into CeO₂ lattice could form a Cu–O–Ce solid solution along with the formation of oxygen vacancies, which promoted the Ce³⁺/Ce⁴⁺ redox cycle and oxygen mobility [23]. Rodriguez et al. [25] have also described that this system with a high catalytic activity had a significant concentration of oxygen vacancies associated with Ce³⁺ cations. Thus, the structural considerations concerning Cu and Ce species were also important for NH₃ oxidation in our work, which could be localized on the catalyst surface, within the subsurface CeO₂ region or adapted the structure of an interstitial Cu–O–Ce solid solution. Generally, preparation methods, such as co-precipitation, impregnation and sol-gel methods, had a strong influence on the physical and chemical properties of Cu–CeO₂ mixed oxides [16], as a consequence, the catalytic performance. Accordingly, taking account of the possible effect on the properties of NH₃ oxidation, we were planning to prepare CuO–CeO₂ mixed oxides with different methods, and investigate the effect of preparation method on the structure/composition and catalytic performance of NH₃ oxidation.

Thus in this paper, the CuO–CeO₂ mixed oxides as potential catalysts for the SCO of ammonia was systematically studied. It was found that the catalyst preparation methods, Cu loading as well as calcination temperature strongly influenced the BET surface area, crystallite sizes and dispersion of CuO species, which in turn strongly affected the catalytic activity. The basic question of structure-activity relationship in CuO–CeO₂ catalyst has also been addressed. More importantly, the roles of finely dispersed CuO, Cu–O–Ce solid solution and CeO₂ species in NH₃–SCO reaction were clearly distinguished.

2. Experimental

2.1. Catalyst preparation

The CuO–CeO₂ catalyst was prepared via a surfactant-templated (ST) method. In the typical procedure, 3.1761 g of cetyltrimethyl ammonium bromide (CTAB) was dissolved in deionized water of 200 ml, followed by the addition 7.5688 g of Ce(NO₃)₃·6H₂O and 1.1406 g of Cu(NO₃)₂·3H₂O. The molar ratio of CTAB/([Cu] + [Ce]) was 0.4. Subsequently, the mixture was stirred for 0.5 h, after which a solution of sodium hydroxide was slowly added under continuous stirring until pH 11. The final precipitate was aged at 90°C for 3 h, washed with deionized water and absolute ethanol until Br species was undetectable by an AgNO₃ solution. Then the obtained solid was dried at 100°C for 12 h, and finally calcined at 500°C for 3 h. The Cu loading amount was 10 wt%. This sample was referred to as 10–CuO–CeO₂ (ST/500). Thus, other CuO–CeO₂ samples with different Cu loading content and calcination temperatures were referred to hereafter as X–CuO–CeO₂ (ST/Y), where X and Y stood for weight percent content of Cu and calcination temperature, respectively.

For comparison, the CuO–CeO₂ catalyst was also prepared by conventional wet impregnation method. Two types of CeO₂ supports were employed: a commercial sample and a prepared sample by the above mentioned surfactant-templated method, which were designated as CuO–CeO₂ (CI) and CuO–CeO₂ (STI), respectively.

2.2. Catalyst characterization

N₂ adsorption/desorption isotherms at about -196°C were obtained using a Quantachrom NOVA-4200e. The specific surface area was calculated using the Brunauer–Emmett–Teller (BET) method. The pore size distributions were determined from desorption branches by the Barrett–Joyner–Halenda (BJH) method.

The powder X-ray diffraction (XRD) experiment was recorded on a Rigaku D/max- γb X-ray diffractometer with monochromatic detector equipped with CuK α radiation. The working voltage was 40 kV, and the current was 100 mA. The samples were scanned from 2θ of 20 – 85° with a step size of 0.02° .

TEM experiments were performed with the JEM-2000EX microscope, using an accelerating voltage of 100 kV. For the TEM analysis, a sample was dispersed in absolute alcohol by an ultrasonic bath and deposited on a Formvar coated 200 mesh Cu grids.

X-ray photoelectron spectroscopy was measured using an X-ray photoelectron spectrometer (ESCALAB 250Xi, Thermo) with a monochromatic X-ray source of Al K α under ultra-high vacuum (3 – 2×10^{-6} Pa). The XPS data from the regions related to the C 1s, O 1s, Cu 2p, Ce 3d, N 1s core levels were recorded for each sample. The binding energies were calibrated internally by the carbon deposit C 1s binding energy (BE) at 284.8 eV. The deconvolution method of XPS spectra was fitted by Gaussian function.

Electron paramagnetic resonance (EPR) measurements were performed at room temperature using a Bruker (A200-9.5/12) operating at the X band (~ 9.8 GHz). The magnetic field was modulated at 100 kHz and the g value was determined from precise frequency and magnetic field values.

H₂ temperature-programmed reduction (H₂-TPR) and the temperature programmed desorption of ammonia (NH₃-TPD) were performed on a Chem BET TPR/TPD Chemisorptions Analyzer. The mass signals of obtained products during NH₃-TPD experiments for N₂ (m/e = 28), N₂O (m/e = 44), NO (m/e = 30), NO₂ (m/e = 46), H₂ (m/e = 2) were recorded using quadrupole mass spectrometer (QMS). Typically, 100 mg of sample was pretreated in a flowing stream of He at 200°C for 1 h. After that, H₂–Ar mixture (10% H₂ by volume) was introduced into the instrument and the temperature was ramped to 1000°C at a heating rate of $10^\circ\text{C}/\text{min}$. The H₂ consumption was monitored by a thermal conduction detector (TCD). For the NH₃-TPD experiments, following the pretreatment step, the catalyst was saturated by a flow of NH₃–He mixture (10% NH₃ by volume). The reactor was then purged with He for a further 2 h to remove weakly adsorbed NH₃. Then He was passed through the reactor and the temperature was ramped from room temperature to 600°C at a rate of $10^\circ\text{C}/\text{min}$.

Temperature programmed surface reaction (TPSR) and NH₃ temperature programmed reaction (NH₃-TPR) experiments were performed in a fixed-bed reactor using a quadrupole mass spectrometer (QMS) as detector. Before the experiment, 100 mg of sample was pretreated in He at 200°C for 60 min. After the sample was cooled to room temperature, the He was switch to a flow of NH₃–He mixture (10% NH₃ by volume) until the QMS showed the stable NH₃ (m/e = 17) intensity. Subsequently, NH₃-TPR experiment was performed at a heating rate of $10^\circ/\text{min}$ under the flow of NH₃. For TPSR experiment, subsequent to the ammonia adsorption, the reactor was purged with He to remove weakly adsorbed NH₃. And then, the He flow was switched to O₂ and the temperature was increased at a rate of $10^\circ/\text{min}$ under the flow of O₂.

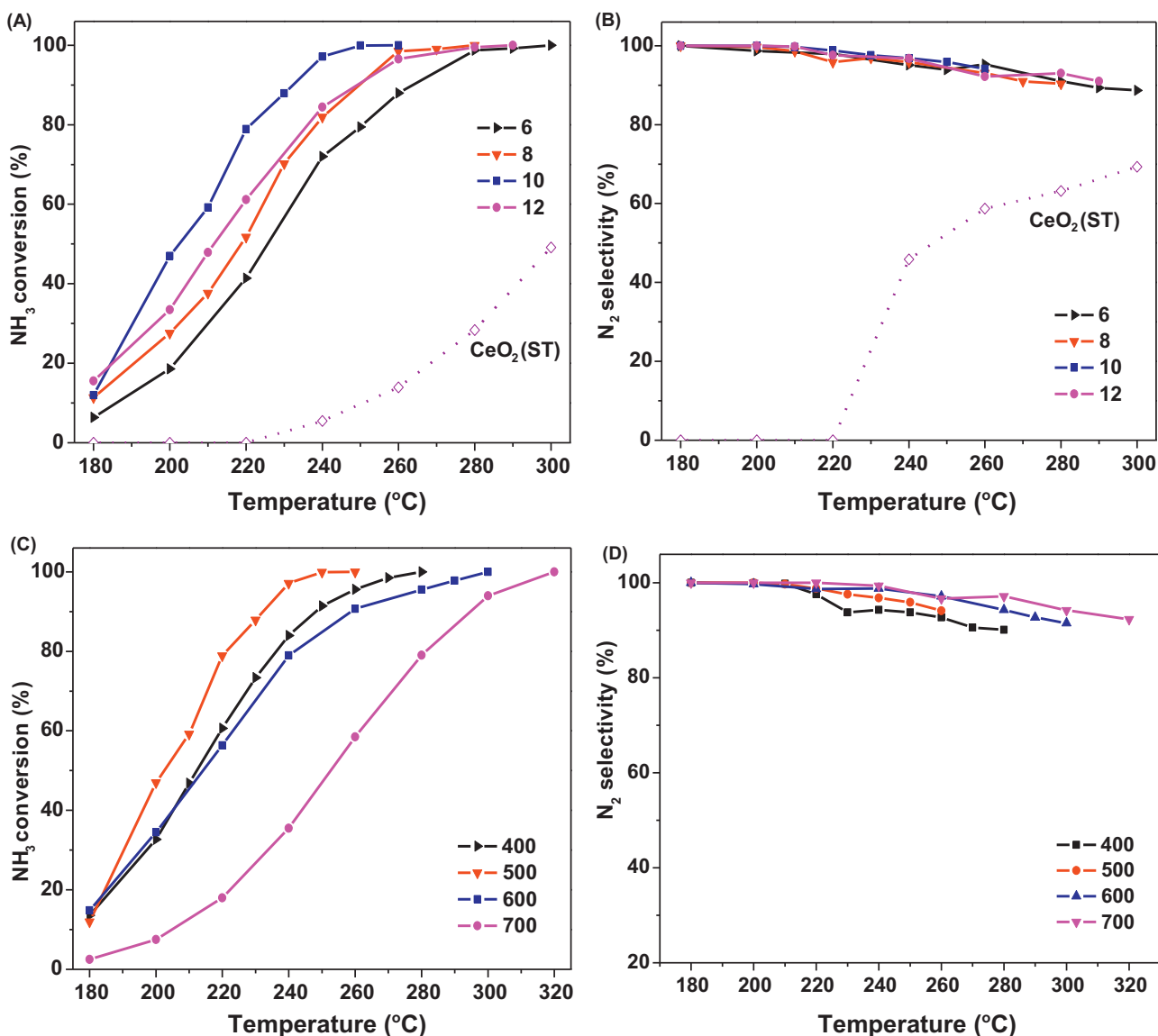


Fig. 1. Effects of Cu doping and calcination temperature on the NH_3 conversion (A, C) and N_2 selectivity (B, D) over X-CuO-CeO_2 (ST/Y) catalysts.

2.3. Catalytic activity tests

The catalytic performance of CuO-CeO_2 catalysts in the selective catalytic oxidation of ammonia (SCO) had been studied in a fixed-bed flow reactor. The composition and amount of the inlet gas mixture were set by mass flow controllers. The typical reactant gas composition was as follows: 1000 ppm NH_3 , 10 vol% O_2 , and balance He. The total flow rate of the reaction mixture was 100 ml/min (gas hourly space velocities (GHSV): $40,000 \text{ h}^{-1}$). The N_2 and NH_3 concentrations were measured using Gas Chromatograph using a 5A column with a TCD detector and the NH_3 analyzer (GXH-1050, Beijing), respectively. The signal of all reactants and possible products were measured at a given temperature at least for 30 min after the reaction had reached a steady state.

3. Results and discussions

3.1. The catalytic performance of CuO-CeO_2 (ST) catalysts

The catalytic performances of CuO-CeO_2 (ST) catalysts with different Cu loadings are showed in Fig. 1A and B. These catalysts were calcined at 500°C in air before reaction. The pristine CeO_2 showed

rather poor NH_3 -SCO activity in the whole temperature range, and it did not exhibit any activity at temperature below 220°C . The NH_3 conversion was only 50% even up to 300°C . Meanwhile, the selectivity of NH_3 oxidation to N_2 was below 70% in the whole temperature range. On the contrary, the CuO-CeO_2 catalysts presented excellent NH_3 -SCO activity in the 180 – 300°C temperature range. From Fig. 1A it could be also seen that the Cu loading showed a significant influence on the catalytic performance. The NH_3 conversion increased significantly with the increase of Cu loading from 6 to 10 wt%, and then it decreased subsequently with the further increase of copper loading from 10 to 12 wt%. The lowest complete ammonia conversion temperature of $\sim 250^\circ\text{C}$ was achieved on 10- CuO-CeO_2 (ST/500) catalyst. Moreover, N_2 was the dominant product of NH_3 oxidation over these series of catalysts. The other products including NO, N_2O and NO_2 were analyzed by MS, and it was found that only a small amount of NO and N_2O was formed with the rise of reaction temperature, and no NO_2 was detected during the activity test. The N_2 selectivity remained above 90% and even reached 100% at lower temperature ($\leq 200^\circ\text{C}$). Thus, the simultaneous enhancement both the catalytic activity and N_2 selectivity for NH_3 oxidation after doping Cu was obtained, which might be due to a synergetic catalytic effect between Cu and Ce species.

Table 1Specific surface areas, cell parameter and crystallite size of CuO–CeO₂ serial catalysts.

Catalysts	BET (m ² g ^{−1})	V ^a (cm ³ g ^{−1})	P ^b (nm)	Cell parameter (nm)	Crystallite size of CeO ₂ ^c (nm)	Particles size of CeO ₂ ^d (nm)
CeO ₂ (ST)	129.8	0.26	6.6	0.5392	7.2	–
6–CuO–CeO ₂ (ST/500)	145.3	0.29	7.4	0.5389	6.1	–
8–CuO–CeO ₂ (ST/500)	147.9	0.24	9.5	0.5386	5.5	–
10–CuO–CeO ₂ (ST/500)	147.1	0.25	6.6	0.5381	5.1	3.7
12–CuO–CeO ₂ (ST/500)	131.4	0.23	6.8	0.5380	5.3	–
10–CuO–CeO ₂ (ST/400)	146.7	0.30	6.2	0.5382	5.2	6.1
10–CuO–CeO ₂ (ST/600)	109.6	0.25	7.0	0.5387	7.4	8.3
10–CuO–CeO ₂ (ST/700)	64.4	0.20	1.1	0.5390	12.8	19.6
10–CuO–CeO ₂ (STI/500)	–	–	–	–	7.9	–
10–CuO–CeO ₂ (CI/500)	–	–	–	–	16.7	–

^a Total pore volume.^b Pore diameter.^c Calculated from the Scherer's equation according to the [1 1 1] diffraction peak of CeO₂.^d Calculated by TEM.

Based on above results, we chose 10 wt% as the optimal Cu doping content and further investigated the effect of calcination temperature (Fig. 1C and D). Increasing the calcination temperature for the catalyst from 400 to 700 °C, a significant influence on the NH₃ conversion under the investigated reaction conditions was observed, particularly at higher temperature (700 °C). Obviously, the catalytic activity of CuO–CeO₂ catalyst increased with the increase of calcination temperature from 400 to 500 °C, and the 10–CuO–CeO₂ (ST/500) clearly exhibited the highest catalytic activity. On the contrary, nontrivial decrease of the NH₃ conversion was found when the calcination temperature was further increased from 500 to 700 °C, and the 10–CuO–CeO₂ (ST/700) catalyst showed the lowest NH₃ conversion. The decrease of catalytic activity at higher calcination temperatures (>500 °C) might be associated with the sintering effect, which would be confirmed by the following XRD, TEM and H₂-TPR analysis. Besides the NH₃ conversion, the selectivity difference of NH₃ oxidation to N₂ was also exhibited in Fig. 1D. The N₂ selectivity showed a slight increase as the calcination temperature increased from 400 to 700 °C. In short, combined with the NH₃ conversion and N₂ selectivity, the optimal calcination temperature for CuO–CeO₂ catalysts was determined to be 500 °C.

3.2. Catalyst characterization

3.2.1. BET surface area, pore structure and XRD

The BET surface area, pore volume and pore diameter are summarized in Table 1. The isotherms of all samples were similar and typical of materials with mesoporosity (pore size was between 6.2 and 9.5 nm) except for 10–CuO–CeO₂ (ST/700) catalyst according to the IUPAC [27]. And the narrow pore size distribution was also exhibited except for 10–CuO–CeO₂ (ST/700) catalyst (not shown here). In addition, all CuO–CeO₂ (ST) catalysts possessed higher surface area (>120 m²/g) except for 10–CuO–CeO₂ (ST/600) and 10–CuO–CeO₂ (ST/700) catalysts. When the calcination temperature rose to 600 °C and 700 °C, the temperature effect became intense and the specific surface area suffered severe decline (109.6 m²/g and 64.4 m²/g). For 10–CuO–CeO₂ (ST/700) catalyst, it also exhibited the smallest pore volume (0.20 cm³ g^{−1}) and pore diameter (1.1 nm), which should be due to the collapse of mesoporous structure at high calcination temperature. Combining with the catalytic activity (Fig. 1), it could be concluded that the special surface area influenced the catalytic performance of CuO–CeO₂ (ST) catalysts, however, the pore characteristic was not directly related with the catalytic activity.

Fig. 2A shows the XRD patterns of CuO–CeO₂ (ST/500) catalysts with different Cu loadings. All the catalysts exhibited the typical patterns of cubic phase of ceria with cubic fluorite structure. No crystalline phase ascribed to CuO or Cu species was observed in

CuO–CeO₂ catalysts with the increasing of Cu loading, suggesting that Cu species existed as the highly dispersed species on the CeO₂ surface, Cu–O–Ce solid solution or a combination of the above two phenomena [15]. Importantly, it was noted that the XRD peaks of CeO₂ became broader and the relative peak intensity became weaker with the increase of Cu loading. In addition, the (1 1 1) diffraction patterns reflections (2θ = 28.5°) of CeO₂ systematically shifted to higher 2θ degree (inset, Fig. 2A), suggesting

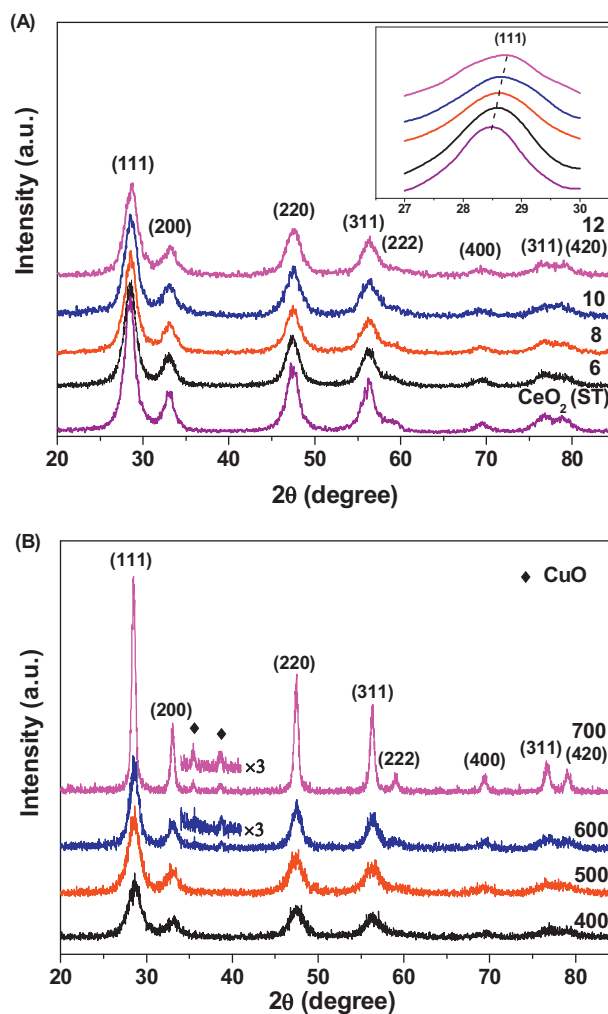


Fig. 2. XRD patterns of (A) X–CuO–CeO₂ (ST/500) catalysts with different Cu loadings (Inset: the enlarged small range (2θ = 27–30°); (B) 10–CuO–CeO₂ (ST/Y) calcined at different temperatures.

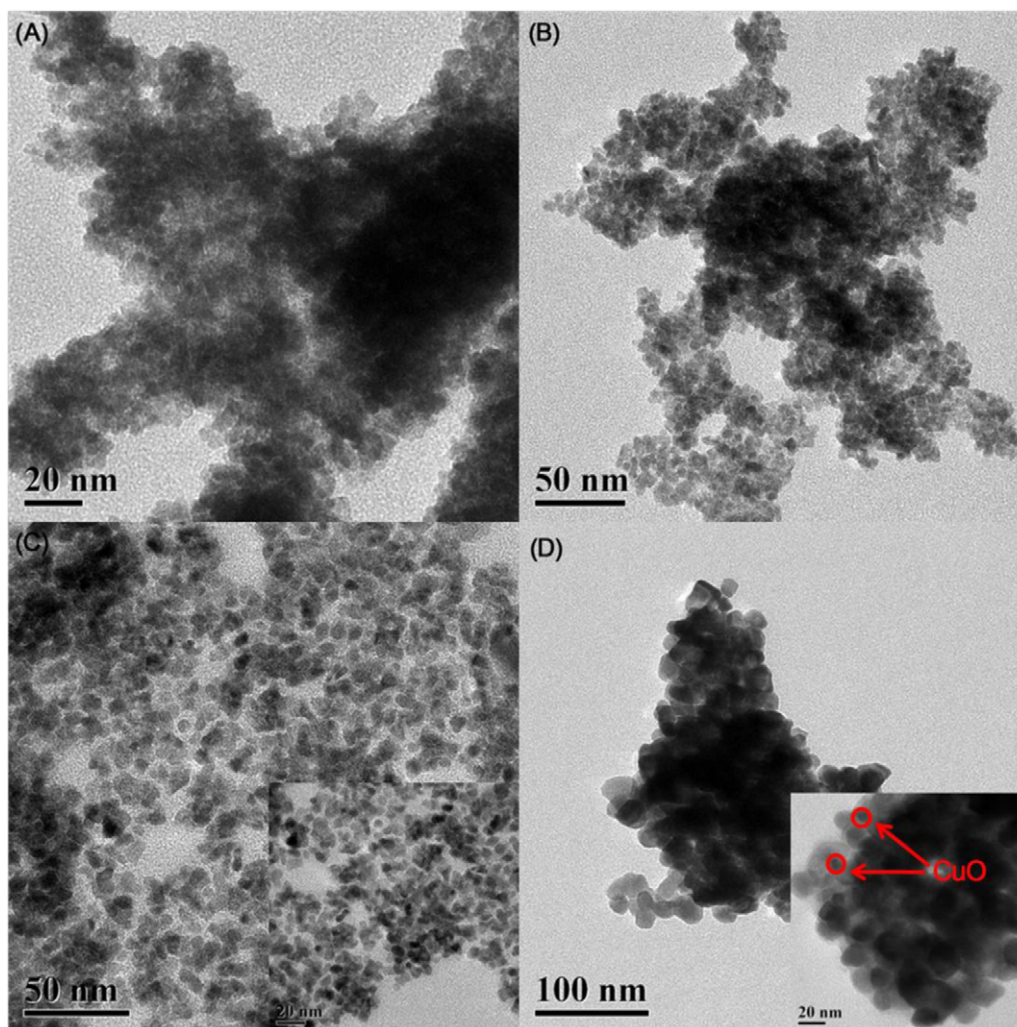


Fig. 3. TEM images of prepared samples of (A) 10-CuO-CeO₂ (ST/400), (B) 10-CuO-CeO₂ (ST/500), (C) 10-CuO-CeO₂ (ST/600), (D) 10-CuO-CeO₂ (ST/700).

that Cu²⁺ has been substituted into the CeO₂ lattice and altered the unit cell parameter of CeO₂ [28] because of the smaller ionic radius of Cu²⁺ (0.72 Å) than that of Ce⁴⁺ (0.97 Å). The decline of lattice parameter calculated by XRD in Table 1 with the addition of Cu compared with pure CeO₂ also evinced above conclusion. More importantly, the lattice parameter data replotted in detail were clearly fitted by a straight line following the Vegard's law (Fig. S1 in the supporting information). Therefore, the identifications of only cubic fluorite phase in XRD patterns and the decrease of the lattice parameter indicated that the copper species have been partly incorporated into the ceria lattice and formed a Cu-Ce-O solid solution [28,29]. Additionally, in comparison with pure CeO₂ (ST), the average crystallite size calculated by using the Scherrer's equation decreased with the Cu loading. Thus the addition of Cu species inhibited the growth of CeO₂ crystallite, and also resulted in the higher BET surface areas (Table 1). The smallest crystallite size of CeO₂ was observed on 10-CuO-CeO₂ (ST/500) catalyst. When the Cu loading increased to 12 wt%, the heterodisperse or aggregation of copper species on the surface of CeO₂ induced the increase of the crystallite size and the decrease of the BET surface area.

Fig. 2B shows the XRD patterns of the 10-CuO-CeO₂ (ST) calcined at different temperatures. With the increase of the calcination temperature, the diffraction peaks of CeO₂ phase became more narrow and intense, as a result of a characteristic change in average crystalline size. In Table 1, it was clear that the high temperature (>500 °C) led to the drastic sintering of the CeO₂ grain, and the

crystalline size of CeO₂ increased from 5.1 nm (500 °C) to 12.8 nm (700 °C). Moreover, when the calcination temperature increased to above 500 °C, the temperature effect also became obvious for Cu species and the XRD peaks corresponding to bulk CuO crystal phases at 35.5° and 38.6° could be observed. Thus it was reasonable to suggest that the low catalytic activity for NH₃ oxidation should be due to the formation of bulk CuO in CuO-CeO₂ catalyst and the aggregation of CeO₂ after the catalyst was calcined at higher temperatures (>500 °C). The appropriate calcination temperature would be favorable to the dispersion of CeO₂ and copper species, and the enhanced catalytic activity.

3.2.2. TEM analysis

The typical TEM images of the prepared 10-CuO-CeO₂ (ST) at different calcination temperatures and the particles sizes of CeO₂ calculated by TEM are shown in Fig. 3 and Table 1, respectively. The 10-CuO-CeO₂ (ST/400) catalyst (Fig. 3A) presented in the form of efficient dispersion and the mean grain diameter of CeO₂ was ~3.7 nm. However, the particle size of CeO₂ increased significantly with the calcination temperature. For the 10-CuO-CeO₂ (ST/500) (Fig. 3B) and 10-CuO-CeO₂ (ST/600) (Fig. 3C), CeO₂ had the mean particle size of ~6.1 nm and ~8.3 nm, respectively. When calcination temperature rose to 700 °C (Fig. 3D), the CeO₂ particles seem to be agglomerated and the mean particle diameter increased to ~19.6 nm. Moreover, the bulk CuO phase was clearly observed in 10-CuO-CeO₂ (ST/700) and the mean diameter was ~8.1 nm. When

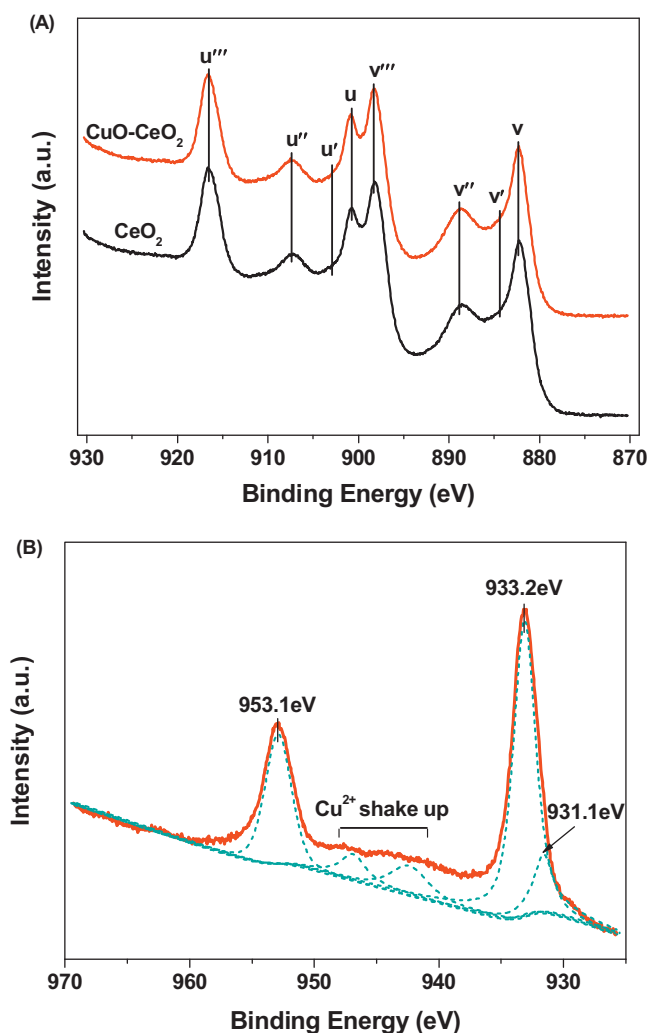


Fig. 4. XPS spectra of (A) Ce 3d and (B) Cu 2p for CeO₂ (ST) and 10-CuO-CeO₂ (ST/500) catalysts.

the calcination temperature was less than 700 °C, it did not clearly observe CuO phase. This above analysis indicated that the particle size was dependent on calcination temperature, which was also in agreement with the result of XRD pattern.

3.2.3. XPS studies

The Ce 3d spectra of 10-CuO-CeO₂ (ST/500) compared with CeO₂ (ST) are shown in Fig. 4A. It was noticeable that the curves of Ce 3d spectra were composed of eight peaks corresponding to four pairs of spin-orbit doublets, suggesting the coexistence of Ce³⁺ and Ce⁴⁺. Moreover, the difference in Ce 3d_{3/2} and Ce 3d_{5/2} binding energies, in accordance with the literatures [30,31], was 18.5 eV. The peaks marked as *u* (901.0 eV), *u''* (907.4 eV) and *u'''* (916.8 eV) were arising from Ce⁴⁺ 3d_{3/2}, while the peaks labeled as *v* (882.5 eV), *v''* (888.9 eV) and *v'''* (898.3 eV) were arising from Ce⁴⁺ 3d_{5/2}. The *u'* (902.9 eV) and *v'* (884.4 eV), referred to 3d_{3/2} and 3d_{5/2}, respectively, were present for Ce³⁺ 3d final state. The surface relative Ce³⁺/Ce⁴⁺ molar ratio was calculated from the normalized peak areas of Ce⁴⁺ and Ce³⁺ core level spectra, as shown in Table 2. There was a slight increase in the Ce³⁺ concentration as copper was incorporated for CuO-CeO₂ catalyst compared with pure CeO₂. In general, the presence of Ce³⁺ was assigned with the generation of oxygen vacancies according to the charge compensation [30,32]. For Cu-Ce system, the evolution of oxygen vacancies was also related to the formation of Cu-O-Ce solid solution [33]. Yet,

Table 2

Surface elemental composition of various catalysts.

Samples	Surface composition (at.%)			Surface element molar ration	
	Ce 3d	Cu 2p	O 1s	O _{latt} /O _{ads}	Ce ³⁺ /Ce ⁴⁺
CeO ₂	39.0	–	61.0	1.12	0.17
CuO-CeO ₂ ^a	28.4	9.7	61.9	1.69	0.19
CuO-CeO ₂ ^b	27.8	9.3	62.9	1.32	0.24
CuO-CeO ₂ ^c	29.5	9.4	61.1	1.26	0.36
CuO-CeO ₂ ^d	29.2	8.0	62.8	1.91	0.23

^a Initial 10-CuO-CeO₂ (ST/500).

^b After the first NH₃-TPR cycle.

^c After the third NH₃-TPR cycle.

^d After treatment by O₂ at 200 °C followed the third NH₃-TPR cycle.

XPS measurements (Fig. 4B) showed that the CuO-CeO₂ catalyst involved a shake-up peak and Cu 2p_{3/2} as well as Cu 2p_{1/2} peaks at 933.2 eV and 953.1 eV, which suggested the presence of CuO species in the catalyst [34]. Notably, a low Cu 2p_{3/2} binding energy at 931.1 eV and the absence of the shake-up peak was characteristic of Cu₂O [35,36]. So it was apparent that Ce⁴⁺, Ce³⁺, Cu²⁺ and Cu⁺ species was coexistence in CuO-CeO₂ catalyst.

3.2.4. H₂-TPR measurements

The H₂-TPR profiles for CuO-CeO₂ (ST) catalysts with different Cu loadings calcined at 500 °C and that calcined at different temperatures are illustrated in Fig. 5A and B, respectively. The pristine CeO₂ exhibited two reduction peaks at about 620 °C and 860 °C, which were attributed to surface and bulk oxygen species reduction, respectively [37]. The reduction of CuO-CeO₂ species took place at much low temperature with complex reduction peaks, which changed with the Cu loadings and calcination temperatures. For the CuO-CeO₂ samples with different Cu contents, two distinct reduction peaks at about 178–193 °C (α) and 227–229 °C (β) were found besides the peak at about 800 °C. A new peak at about 264–266 °C (γ) also appeared when calcination temperature reached to 600 and 700 °C besides peak α (183–203 °C) and peak β (210–231 °C).

Taking into consideration the XRD and XPS analyses, it was more likely that the α peak was attributed to the finely dispersed CuO species strongly interacting with ceria surface, peak β was assigned to the reduction of Cu²⁺ ions in Cu-Ce-O solid solution [38] and the peak γ was related to the reduction of bulk CuO confirmed by XRD patterns of 10-CuO-CeO₂ (ST/600) and 10-CuO-CeO₂ (ST/700) samples [35]. Additionally, from Fig. 1D it was clearly seen that the 10-CuO-CeO₂ (ST/600) and 10-CuO-CeO₂ (ST/700) outperformed the 10-CuO-CeO₂ (ST/400) and 10-CuO-CeO₂ (ST/500) in terms of N₂ selectivity. Such phenomenon might be mainly associated with the bulk CuO species, which exhibited the worse reducibility. Chemielarz et al. [4] and Slavinskaya et al. [39] have proposed that the strength of oxygen bonding in metal oxidation determined the distribution of ammonia oxidation products. The higher was the oxygen bonding strength, the better was N₂ selectivity. This was consistent with the sequences of our N₂ selectivity and reducibility revealed by the H₂-TPR investigations. The similar N₂ selectivity for CuO-CeO₂ (ST/500) with different Cu loadings also proved it. A quantitative analysis on H₂ consumption calculated by integrating the H₂-TPR curves is reported in Table 3. Obviously, the $\alpha/(\alpha + \beta + \gamma)$ molar ratio decreased in the order of 10-CuO-CeO₂ (ST/500, 0.59) > 12-CuO-CeO₂ (ST/500, 0.52) > 8-CuO-CeO₂ (ST/500, 0.50) > 6-CuO-CeO₂ (ST/500, 0.47) in the various Cu loadings, coinciding with the sequences of catalytic performance in Fig. 1A. Furthermore, for the 10-CuO-CeO₂ (ST) catalysts calcined at different temperatures, the sequence of $\alpha/(\alpha + \beta + \gamma)$ molar ratio was also accordance with the NH₃ conversion. That was to say, the higher molar ratio of the finely dispersed CuO species was

Table 3The quantitative TPR analyses of the CuO–CeO₂ catalysts.

Catalyst	Peak temperature (°C)			H ₂ consumption ^a (μmol/g-cat)			H ₂ consumption ratio peak $[\alpha/(\alpha + \beta + \gamma)]$
	α	β	γ	α	β	γ	
6-CuO–CeO ₂ (ST/500)	178	227	–	418.7	466.4	–	0.47
8-CuO–CeO ₂ (ST/500)	188	229	–	530.3	528.1	–	0.50
10-CuO–CeO ₂ (ST/500)	192	229	–	731.7	498.2	–	0.59
12-CuO–CeO ₂ (ST/500)	193	229	–	728.4	672.3	–	0.52
10-CuO–CeO ₂ (ST/400)	183	210	–	478.8	578.2	–	0.45
10-CuO–CeO ₂ (ST/600)	191	220	264	403.1	516.9	290.3	0.33
10-CuO–CeO ₂ (ST/700)	203	231	266	345.7	410.5	508.4	0.27
10-CuO–CeO ₂ (STI/500)	201	–	245	381.7	–	951.8	0.28
10-CuO–CeO ₂ (CI/500)	199	–	246	300.1	–	968.0	0.23

^a Calculated by equation: $Y = 0.029X - 1.823$, $R^2 = 0.996$, $S^2 = 0.5963$, and X, Y referred to the area of each reduction peak and the H₂ consumption, respectively.

advantageous to promote the NH₃–SCO activity. The formation of the finely dispersed CuO species strongly interacting with ceria surface should be the key factor for the enhanced catalytic activity.

3.2.5. EPR analysis

EPR has been reported to be very effective technology to identify paramagnetic Cu²⁺ species in the catalysts, even in a trace amount [40]. Detailed studies of copper-based catalysts generally revealed the existence of two types of copper species: (i) isolated Cu²⁺

ions incorporated into or on the catalyst surface and localized in tetrahedral or octahedral sites; (ii) CuO clusters or particles irregularly distributed on the catalyst surface [41]. Fig. 6 presents the room-temperature EPR spectra of 10-CuO–CeO₂ (ST/500) catalyst. The EPR spectra clearly evidenced that four types of paramagnetic copper species denoted A₁, A₂, O and K could be identified. Two signals, A₁ and A₂, were corresponded to isolated monomeric Cu²⁺ ions in sites with an axial symmetry environment. The central A₁ signal around at $g_{||} = 2.240$ and $g_{\perp} = 2.036$ composed of four narrow hyperfine splitting in its parallel and perpendicular components with $A_{||} = 170$ G and $A_{\perp} = 25$ G, which was attributed to Cu²⁺ ion monomers in octahedral sites with a tetragonal distortion [42]. The above XRD results also proved the presence of structure distortion due to the addition of Cu species (Fig. 2A and Table 1). The signal A₂ with well-resolved hyperfine structure at least in the parallel component was observed, and the perpendicular features was unresolved. The EPR parameters of that signal was $g_{||} = 2.107$ and $A_{||} = 81$ G, suggesting the presence of Cu²⁺ ions localized in surface substitutional lattice sites with a square-pyramidal symmetry. A broad signal ($g = 2.091$, $\Delta H \approx 950$ G) with an asymmetric lineshape, denoted O, was detected to be overlapped with other three signals (A₁, A₂ and K). This signal was similar to that reported previously [43,44] and corresponded to Cu²⁺ ions in the presence of strong magnetic dipolar interaction. Kaïs et al. [45] have shown that this signal was obtained in CuO particles, and the g value about 2.095 and the asymmetric line shape was typical of the Cu²⁺ ions signal in the amorphous oxides. It has been known the presence of CuO species in CuO–CeO₂ catalyst from XPS analysis. Thus the finely dispersed CuO particles should be responsible for the O signal.

Most notably, the signal K is also observed in CuO–CeO₂ catalyst and ascribed to copper (II) ion dimers. Indeed, the symmetrical fine structure doublets composed of seven lines with relative intensities 1:2:3:4:3:2:1 was observed in the parallel ($g_{||} = 2.217$, $A_{||} = 85$ G) and perpendicular ($g_{\perp} = 2.042$, $A_{\perp} = 13$ G) components (Fig. 6). Such type structure was produced by the coupling between two identical nuclei Cu²⁺ of spin $I = 3/2$ [45]. Additionally, a weak signal corresponding to the forbidden spin transition ($\Delta m_s = 2$), could be obtained at just half the normal magnetic field intensity. On the other hand, the signal observed at the normal magnetic field was correlated with the allowed transition ($\Delta m_s = 1$) [29]. The fine structure of the spectrum and the presence of the half magnetic field signal were characteristic of the copper (II) ion dimers. The hyperfine splitting constants ($A_{||} = 170$ G and $A_{\perp} = 25$ G) of A₁ signal was nearly double than those of the K signal, and also showed the similar g tensor values. Thus it was thought that these Cu²⁺ monomers were the precursor of the Cu²⁺ dimers in ceria and must have the same environment symmetries as the two Cu²⁺ ions presented in dimers [46]. And it was necessary to discuss the relative positions of the Cu²⁺ dimers involved in the CeO₂ structure. According to the equation reported by Eaton et al. [47,48], the

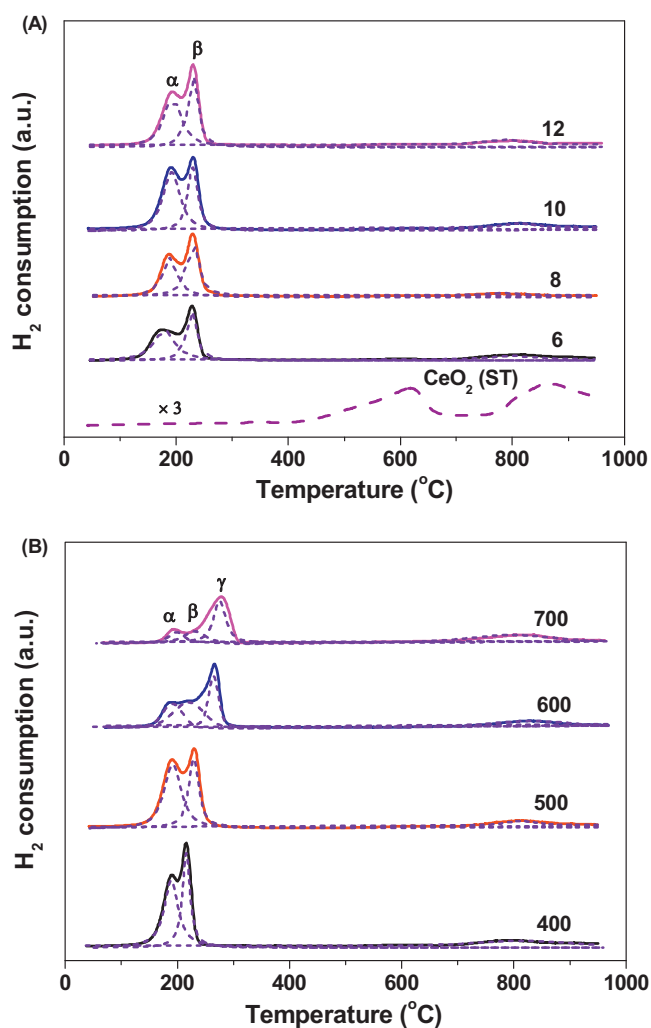


Fig. 5. H₂-TPR profiles of (A) X-CuO–CeO₂ (ST) catalysts calcined at 500°C with different Cu loadings; (B) 10-CuO–CeO₂ (ST/Y) catalysts calcined at different temperatures.

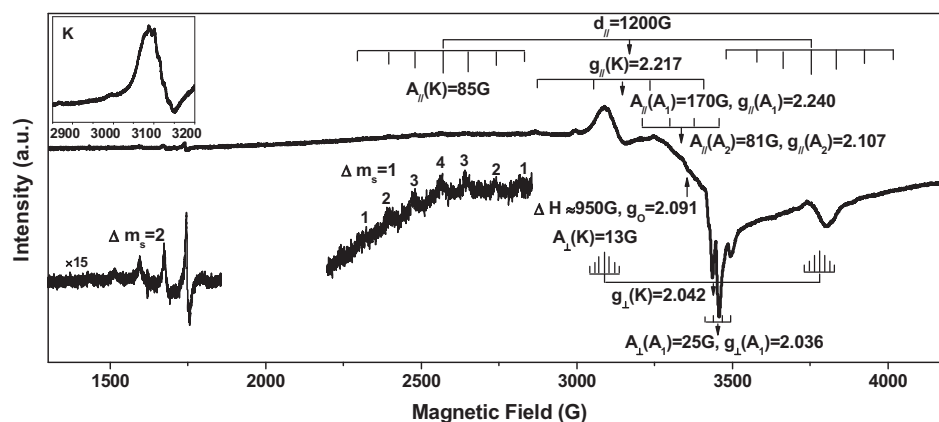
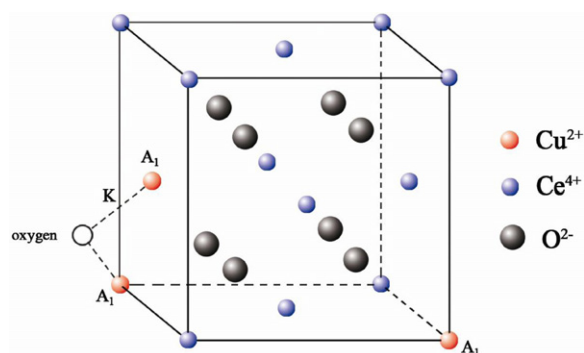


Fig. 6. EPR spectra recorded at room temperature of 10-CuO-CeO₂ (ST/500). Inset: the enlarged at the range of 2850–3200 G.

inter-ion distance between the two Cu²⁺ ions forming the dimers has been calculated to be 3.5 Å. Since the shortest separation distance between two neighboring Ce⁴⁺ in the lattice was 3.811 Å, which was near the calculated distance, then it was possible that such Cu²⁺ ions was located by substitution of two Ce⁴⁺ in neighboring positions. Moreover, it could also provide an additional evidence for structure distortion of CeO₂ during Cu²⁺ ions incorporation into CeO₂ lattice (3.5 Å < 3.811 Å). The relative position of Cu monomers (A₁) as precursors of Cu²⁺ dimers and the formed Cu²⁺ dimers (K) in CeO₂ structure in the presence of O₂ participation has been expressly shown in Scheme 1. Simultaneously, the appearance of signal K also provided predominant evidence on the formation of partial Cu-Ce-O solid solution, which was in good accordance with above XRD and XPS results.

3.3. Comparison of CuO-CeO₂ (STI) with CuO-CeO₂ (CI) catalysts

To better evaluate the catalytic performance of 10-CuO-CeO₂ (ST/500) catalyst, the comparative NH₃-SCO activity tests over 10-CuO-CeO₂ (STI/500) and 10-CuO-CeO₂ (CI/500) catalysts were also carried out (Fig. 7). Obviously, the CuO-CeO₂ (STI) and CuO-CeO₂ (CI) catalysts were inferior to CuO-CeO₂ (ST) catalyst in catalytic performance, and the corresponding 100% conversion temperatures (*T*₁₀₀) were 275 °C, 305 °C and 250 °C, respectively. Furthermore, the NH₃ conversion obtained over our CuO-CeO₂ (ST) catalysts were, on average, 25% higher than those achieved on Cu-Ce catalyst prepared by co-precipitation under the same test conditions in the 200–340 °C range [21]. Hence, the catalyst preparation methods showed a remarkable influence on the catalytic activity of Cu-Ce catalysts, where the surfactant-templated method gave Cu-Ce catalysts an excellent catalytic performance for NH₃ oxidation.



Scheme 1. A model of the relative position of one Cu monomer (A₁) and one Cu dimer (K) in the ceria lattice.

Compared with CuO-CeO₂ (ST) catalyst, two small diffraction peaks at $2\theta = 35.5^\circ$ and 38.7° , which was ascribed to bulk CuO species, were visible on CuO-CeO₂ (STI) and CuO-CeO₂ (CI) catalysts (Fig. 8). The XRD patterns of CeO₂ in the samples CuO-CeO₂ (STI)

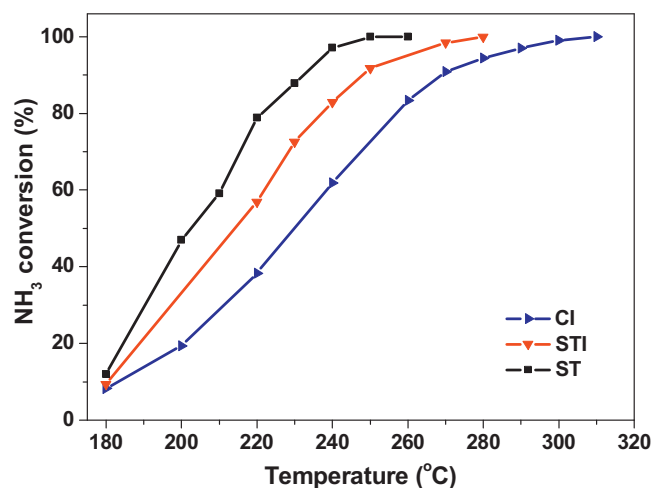


Fig. 7. Comparison of NH₃ conversion for 10-CuO-CeO₂ (ST/500), 10-CuO-CeO₂ (STI/500) and 10-CuO-CeO₂ (CI/500) catalysts.

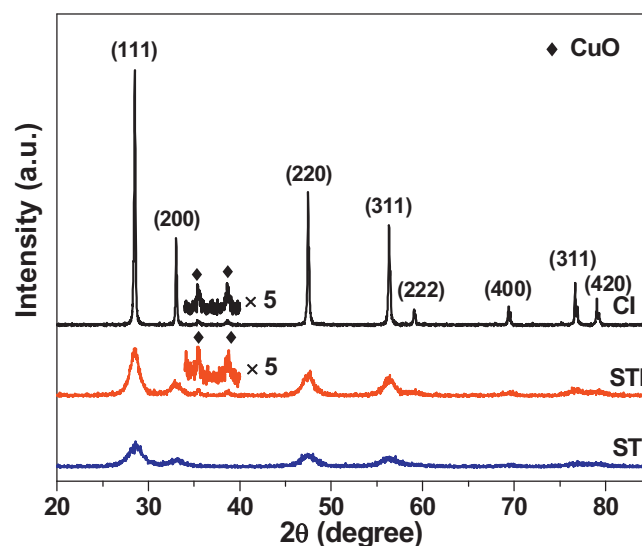


Fig. 8. XRD patterns at wide diffraction angles of 10-CuO-CeO₂ (ST/500), 10-CuO-CeO₂ (STI/500) and 10-CuO-CeO₂ (CI/500) catalysts.

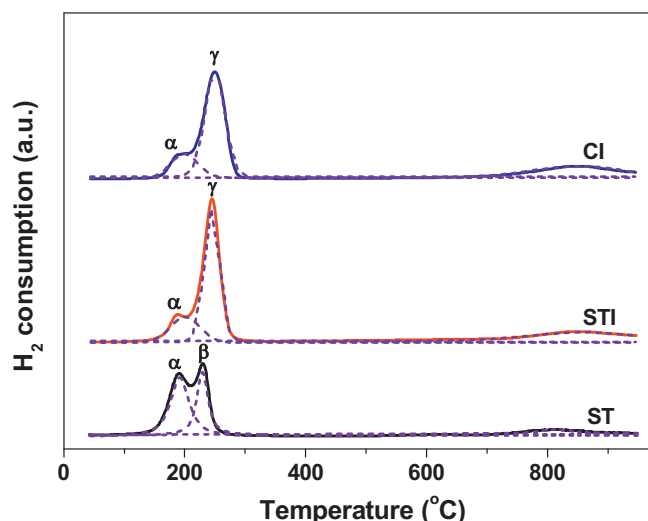


Fig. 9. H₂-TPR profiles of 10-CuO-CeO₂ (ST/500), 10-CuO-CeO₂ (STI/500) and 10-CuO-CeO₂ (CI/500) catalysts.

and CuO-CeO₂ (CI) became sharp and narrow. The CeO₂ crystallite size was about 7.9 and 16.7 nm for the samples CuO-CeO₂ (STI) and CuO-CeO₂ (CI), respectively, which were great larger than that of CuO-CeO₂ (ST), as shown in Table 1. Fig. 9 shows the H₂-TPR profiles of CuO-CeO₂ prepared by different method. The peak γ assigned to bulk CuO particles has been observed on the CuO-CeO₂ (STI) and CuO-CeO₂ (CI) samples, which was consistent with the XRD results. The formation of bulk CuO species was not beneficial for the activity. No peak β was observed for the two samples, which indicated that Cu-O-Ce solid solution species was not formed in the ceria by the impregnation method. Meanwhile the decrease of α/(α + β + γ) molar ratio on the CuO-CeO₂ (STI) and CuO-CeO₂ (CI) samples also indicated the decrease of the amount of highly dispersed CuO species on the catalysts (Table 3). The direct relationship between the quantification of α/(α + β + γ) molar ratio and catalyst activity is exhibited in Fig. 10. The higher α/(α + β + γ) molar ratio was, the lower complete conversion temperature became. The strong synergistic effect between CuO and CeO₂ in ammonia oxidation was obtained. The finely dispersed CuO species supported on smaller CeO₂ was in favorable to the higher activity for NH₃ oxidation. And the surfactant-templated method was also a potential candidate to prepare CuO-CeO₂ catalysts for the catalytic removal of NH₃.

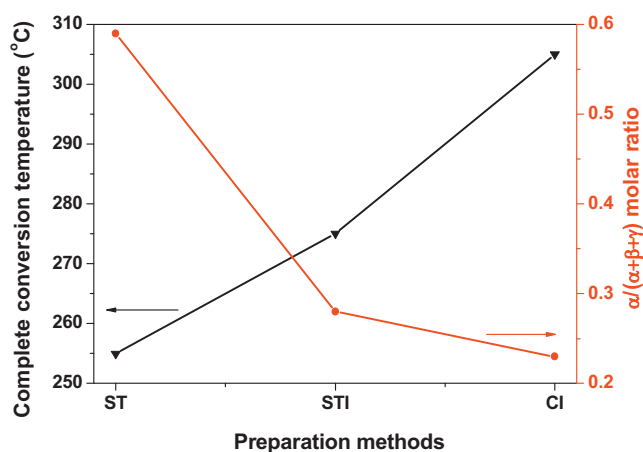


Fig. 10. Variations of temperature for NH₃ complete conversion and the α/(α + β) molar ratio with the different preparation methods.

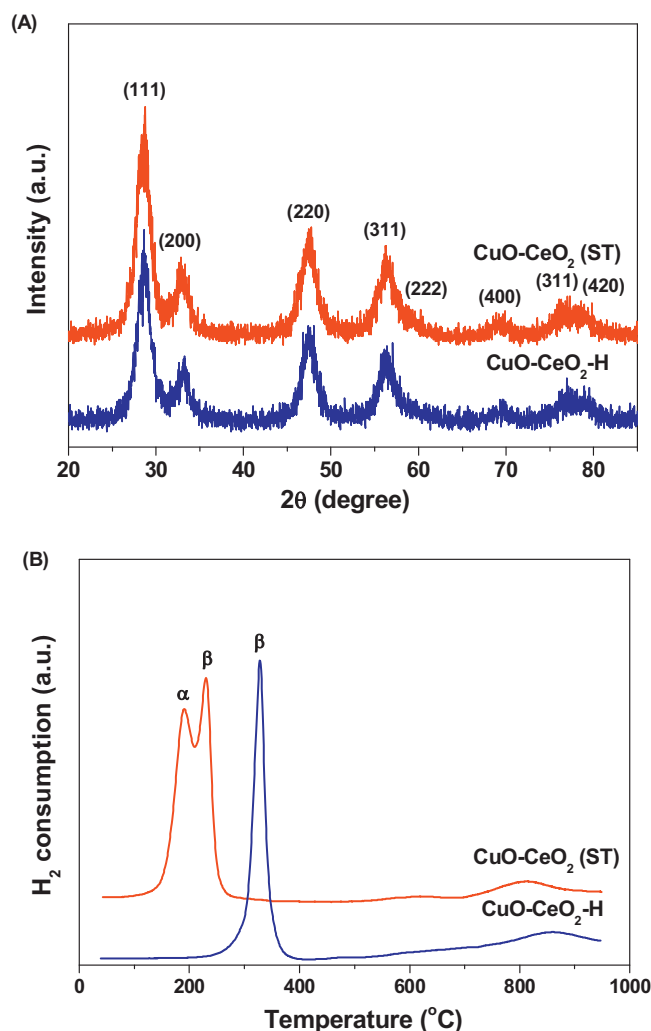


Fig. 11. XRD patterns (A) and H₂-TPR profiles (B) of CuO-CeO₂ (ST) and CuO-CeO₂-H catalysts.

3.4. Roles of finely dispersed CuO, Cu-O-Ce solid solution and CeO₂ species in NH₃ oxidation

3.4.1. Comparison of CuO-CeO₂ and CuO-CeO₂-H catalysts

The mechanism of the synergistic effect of Cu and Ce species during NH₃-SCO reaction will be further discussed in the following part. In the present work, the finely dispersed CuO, Cu-O-Ce solid solution and CeO₂ species coexisted in the 10-CuO-CeO₂ (ST/500) sample. The finely dispersed CuO has been proved to be useful for the activity. In order to well prove the effect of highly dispersed CuO during the reaction, in this work, the 10-CuO-CeO₂ (ST/500) catalyst was treated by concentrated nitric acid (50% HNO₃), and this catalyst was designated CuO-CeO₂-H. XRD analysis of CuO-CeO₂-H suggested no significant disparity after the acid treatment, implying that the intrinsic structure of CuO-CeO₂ catalyst was not altered (Fig. 11A). The H₂-TPR analysis (Fig. 11B) indicated that the peak α assigned to finely dispersed CuO disappeared for CuO-CeO₂-H. The finely dispersed CuO species could be easily eliminated by nitric acid. Only one H₂ reduction peak at higher temperature corresponding to Cu species was observed, which was reasonably suggested to be the reduction of Cu²⁺ ions in the Cu-O-Ce solution solid (peak β) since no XRD patterns attributed to CuO crystal phase was observed. Nevertheless, the position of the peak β clearly shifted toward higher temperature, which should be due to the absence of the hydrogen spillover [49]. In general, when the finely

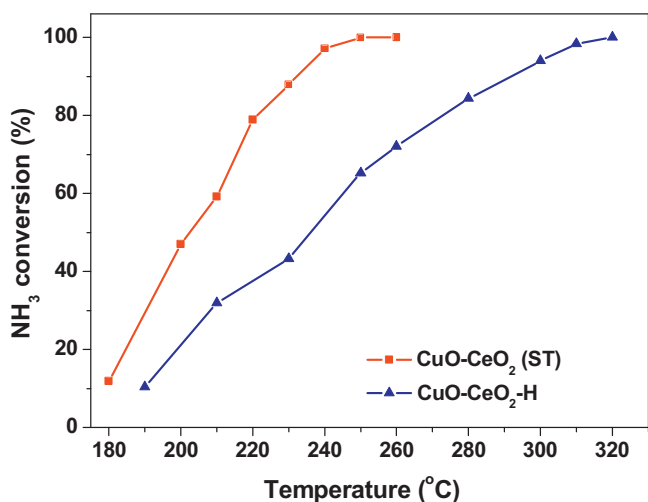


Fig. 12. NH₃ conversion over CuO-CeO₂ (ST) and CuO-CeO₂-H catalysts.

dispersed CuO species existed on the catalysts and was reduced in H₂-TPR measurement, the atomic hydrogen generated by dissociative adsorption on the metallic Cu⁰ surface could spill over onto the surface of lattice Cu²⁺ ions in the Cu-O-Ce solution solid, and thereby decreased its reduction temperature. Accordingly, after the finely dispersed CuO was removed by nitric acid, the reduction temperature of peak β reasonably increased to higher temperature. Notably, for CuO-CeO₂-H catalyst (Fig. 12), there was a drastic fall in the activity compared with the original CuO-CeO₂ catalyst. Therefore, the above results directly evidenced that the finely dispersed CuO species was more efficient active sites for the NH₃-SCO reaction.

3.4.2. The determination of ammonia adsorption and activation sites in NH₃-SCO reaction

In order to determinate the ammonia adsorption and activation sites, and achieve the detailed reason for the activity enhancement of NH₃ oxidation, the temperature programmed desorption of ammonia (NH₃-TPD) technique was carried out. In Fig. 13, the ammonia desorbed at lower temperature (~100 °C) may be assigned to physically adsorbed NH₃, while another one at higher

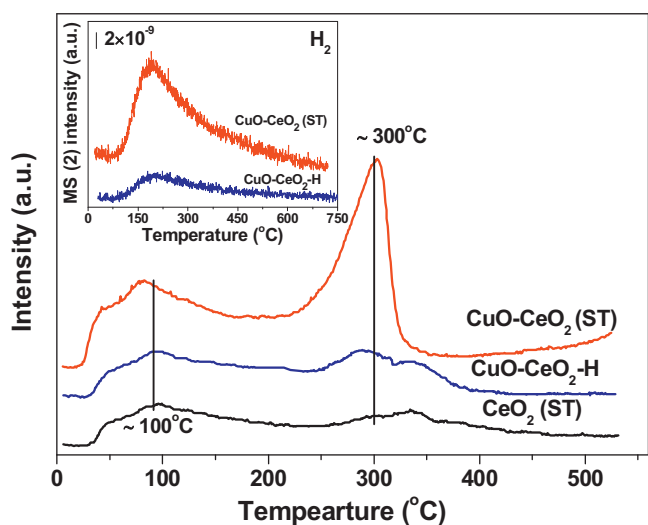
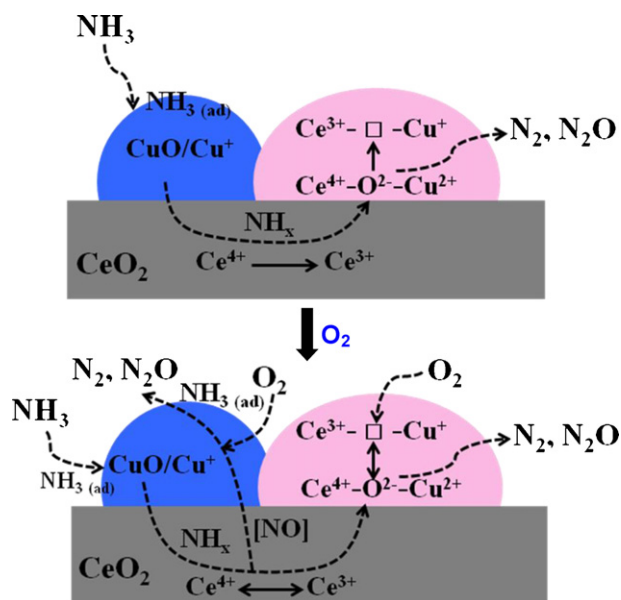


Fig. 13. TPD profiles of ammonia over CeO₂ (ST), CuO-CeO₂ (ST) and CuO-CeO₂-H catalysts (inset: formation profile of H₂ over CuO-CeO₂ (ST) and CuO-CeO₂-H catalysts during NH₃-TPD experiment).

temperature (~300–350 °C) was related to the chemisorbed NH₃ [8]. As evident from the results in Fig. 13, the desorption amount of chemisorbed NH₃ on the surface of the CuO-CeO₂ (ST/500) catalyst with finely dispersed CuO species was intensively greater than those on CeO₂ (ST) and CuO-CeO₂-H catalysts. Thus it was reasonable to conclude that the finely dispersed CuO species was the main adsorption sites of NH₃ molecules. Additionally, in parallel with the NH₃ desorption, the formation of H₂ and N₂ at low temperatures on CuO-CeO₂ (ST/500) catalyst during the NH₃-TPD experiment suggested that some adsorbed NH₃ may be further activated to form NH_x species, and then decompose to N₂ and H₂ (inset in Fig. 13 and Fig. S2). Subsequently, the reaction of chemisorbed NH_x species with oxygen species in CuO-CeO₂ catalyst formed N₂O, N₂, and H₂O at 200–400 °C (Fig. S2) [3,50].

Though it was confirmed that NH₃ molecules was mainly adsorbed on the finely dispersed CuO species, it was necessary to determine the activation sites of NH_{3(ad)} to NH_x in NH₃ oxidation reaction. Ramis et al. have studied the behavior of adsorption, activation and oxidation of ammonia over SCR catalysts, and they found that the surface reaction of ammonia activation was slow by reduction of Cu (II) to Cu (I) though the adsorption of ammonia also occurred over the supported copper oxides [51]. In our work, XPS results have clearly stated that CuO-CeO₂ (ST) catalyst performed excellent reversible Ce³⁺/Ce⁴⁺ redox capability. Adamowska et al. [52] also reported that the reversible Ce³⁺/Ce⁴⁺ could be maintained even after exposure to the reduction condition. More importantly, in parallel with the NH₃ desorption, the H₂ formation could also be observed during NH₃-TPD experiment over ceria-zirconia mixed oxides in our previous study, which indicated that some NH₃ could be further activated and transformed into NH_x species on such mixed oxides [3]. Such role of CeO₂ was some similar formulated RuO₂, which could adsorb and activate NH₃ molecules in CuO/RuO₂ catalyst for NH₃-SCO [53,54]. The NH_{3(ad)} was activated to NH_x by the reversible Ce³⁺/Ce⁴⁺ redox property. In addition, it has been known that the disappearance of the finely dispersed CuO species (CuO-CeO₂-H) would result in the amount decrease of H₂ production during NH₃-TPD experiment (inset in Fig. 13) and the lower NH₃ conversion (Fig. 12). Thus it was thought that the copper species should also play an important role in activating NH₃ besides ceria species, and the activation process of NH_{3(ad)} was accomplished by the synergetic interaction between copper and ceria species. A stronger synergetic interaction between the ceria with smaller crystallite size and the finely dispersed CuO species was observed in CuO-CeO₂ (ST/500) catalyst, which promoted the NH₃ activation and NH₃-SCO reaction. The similar result has also been reported by Luo et al. [55], it was found that the synergetic effect could be strengthened from higher component dispersion and smaller crystallite size in CuO-ZrO₂ catalyst, which provided much more active centers for the catalytic activity. Meanwhile, the generation of Cu⁺ together with observation of Ce³⁺ species in XPS spectra was indicative of the redox equilibrium (Cu⁺ + Ce⁴⁺ ↔ Cu²⁺ + Ce³⁺) [56]. The quick change of chemical state in near-surface region in CuO-CeO₂ catalyst and the strong electron state interaction greatly contributed the process of ammonia activation by ceria, which was one reason for the enhanced catalytic activity of CuO-CeO₂ (ST) catalysts. In one word, the adsorbed NH₃ on the finely dispersed CuO could be transferred on the surface of CeO₂ under the interface interaction between copper and ceria species, which was further activated and transformed into NH_x type species by ceria under the rules of quick change of chemical state in near-surface region and the strong electron state interaction in CuO-CeO₂ catalysts, as shown in Scheme 2.

Fig. 14 shows the temperature programmed surface reaction (TPSR) between adsorbed NH₃ and gaseous oxygen. At moderate temperature (~250 °C), apart from the N₂ and N₂O production, some NO were also produced. And the amount of all products



Scheme 2. Reaction models of NH_3 oxidation on CuO-CeO_2 (ST) catalyst.

was larger than that obtained from NH_3 -TPD. Interestingly, it was clearly seen that the NO production peak at $\sim 250^\circ\text{C}$ was broader (100 – 400°C) and unsymmetrical. The NO was the key intermediate in the 100 – 400°C temperature range during TPSR experiment, which suggested that the “internal” selective catalytic reduction (iSCR) mechanism could be present in CuO-CeO_2 catalyst during the NH_3 -SCO reaction [2,57]. The catalytic activity in the selective catalytic reduction of NO with ammonia (NH_3 -SCR) over our CuO-CeO_2 catalyst (Fig. S3) provided an additional evidence for the (iSCR) mechanism in NH_3 -SCO [50]. Zheng et al. [58] demonstrated that the formation of N_2 and N_2O could be related to the dissociative desorption of NO on oxygen vacancies in CeO_2 . Many literatures have also demonstrated that CuO species was active in the reduction of NO into N_2 during ammonia oxidation [57,59]. Thus, it was suggested that the activation of ammonia by ceria led to the formation of N_2 and NO_x , followed by the oxidation between NO and $\text{NH}_3(\text{ad})$ selectively catalyzed by CuO to N_2 [60]. This was also consistent with our conclusion in Section 3.2.4 that CuO phase could affect N_2 selectivity in NH_3 oxidation over CuO-CeO_2 catalysts. At

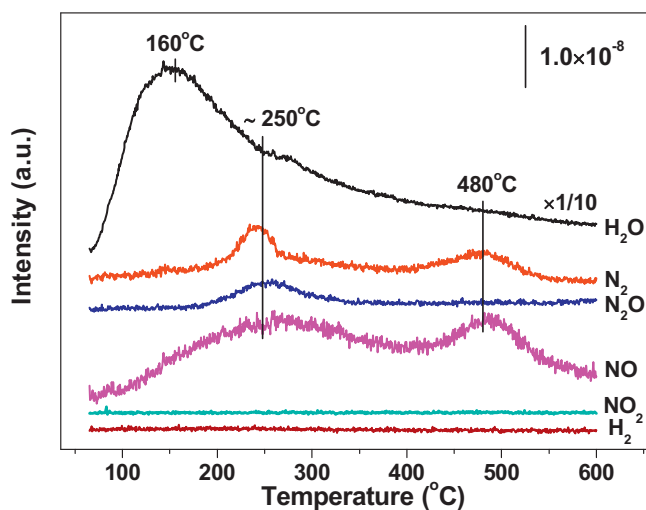


Fig. 14. Results of temperature programmed surface reaction (TPSR) for 10-CuO-CeO_2 (ST/500) catalyst.

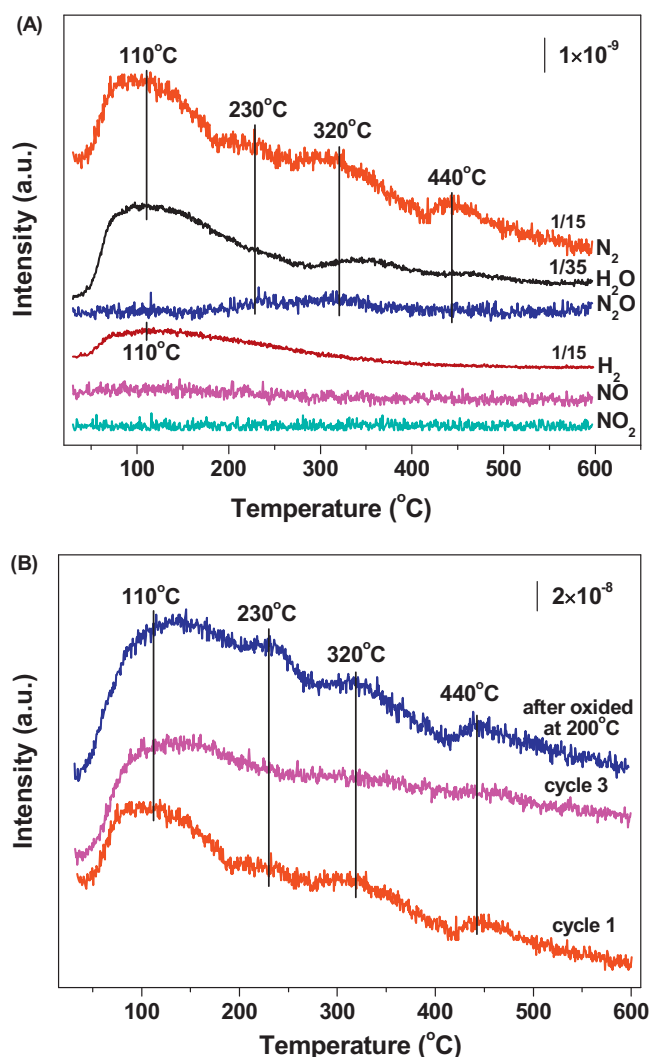


Fig. 15. Results of NH_3 temperature programmed reaction (NH_3 -TPR) profiles (A) and N_2 production profiles during NH_3 -TPR cycles (B) of 10-CuO-CeO_2 (ST/500) catalyst.

higher temperature (480°C), no production of N_2O was observed, and the NO was formed as by product instead of N_2O [61].

3.4.3. The TPR of ammonia on CuO-CeO_2 catalyst

Fig. 15A shows the NH_3 temperature programmed reaction (NH_3 -TPR) profiles on 10-CuO-CeO_2 (ST/500) catalyst. Apart from the formation of N_2 and N_2O , no NO and NO_2 were produced during the NH_3 -TPR. Such diversity proved that the reaction pathway during NH_3 -TPR could differ from the process of TPSR. There were four N_2 production maxima at 110°C , 230°C , 320°C and 440°C , respectively. Our previous studies [3] have already revealed that the N_2 formation did not originate from the physically adsorbed N_2 . The analysis of $\text{N}1s$ region in XPS spectra also demonstrated that no nitrate was observed on the oxide surface (Fig. S4), suggesting it has been completely removed during the calcinations. So the N_2 and N_2O formation was also not correlated with the decomposing of residual nitrate. The N_2 formation centered at 110°C should be due to the combination of two NH_x species by the following reaction of ($2\text{NH}_x \rightarrow \text{N}_2 + 2x\text{H}^+ + 2xe^-$) [3,62]. The N_2 formation at 230°C was caused by the reaction of NH_3 with surface adsorbed oxygen ions [63]. The latter two N_2 formation peaks (320°C , 440°C) were created by the reaction of ammonia with lattice oxygen [64]. Moreover it can be found that the main product was N_2 and H_2O for

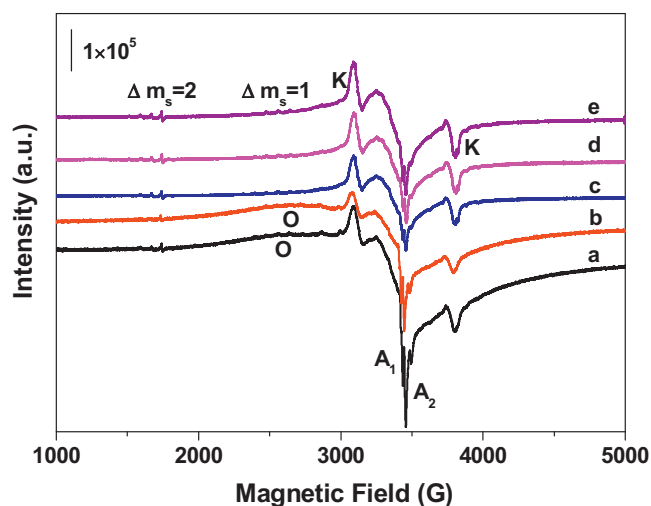
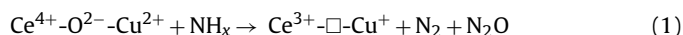


Fig. 16. The EPR spectra recorded at room temperature of 10-CuO-CeO₂ (ST/500) after the following treatments: (a) initial sample; (b) reduction at 200 °C up passing NH₃ for 10 min; (c) oxidation at 200 °C up passing O₂ for 10 min after (b); (d) reaction in NH₃ + O₂ at 200 °C for 10 min; (e) reaction in NH₃ + O₂ at 260 °C for 10 min.

the reaction of NH₃ with oxygen species in CuO-CeO₂ catalyst. In order to more precisely determine the change of oxygen species, the successive cycles of the NH₃-TPR were also carried out on the CuO-CeO₂ (ST/500) catalyst (Fig. 15B). During the three successive cycles, the low-temperature peak at 110 °C always existed in the NH₃-TPR. However, the formation peak of N₂ at 230 °C gradually disappeared, and only few amount of N₂ formation at 320 °C and 440 °C was observed in the third cycle. It was noticed that the lattice oxygen was gradually consumed in NH₃-TPR cycles. After the third NH₃-TPR cycle, the CuO-CeO₂ catalyst was treated in gaseous oxygen at 200 °C again, and then the NH₃-TPR experiment was carried out. It could be found that the production peaks for N₂ at 230 °C, 320 °C and 440 °C have been restored compared with the first NH₃-TPR cycle. NH₃ could react with adsorbed oxygen on the surface of CuO-CeO₂ sample and the lattice oxygen in the catalyst. When these oxygen species (adsorbed oxygen and lattice oxygen) were consumed during NH₃-TPR experiment, gaseous oxygen can refill these consumed oxygen species and constitute the oxygen cycle, and meanwhile the activity for ammonia oxidation was promoted.

3.4.4. EPR and XPS investigation of CuO-CeO₂ catalyst in ammonia oxidation

The EPR spectra of 10-CuO-CeO₂ (ST/500) samples after redox treatment with O₂ or/and NH₃ are shown in Fig. 16. When the CuO-CeO₂ sample was exposed to ammonia at 200 °C, the line shape of EPR spectra (Fig. 16(b)) did not exhibit visible change, but a significant diminution of the K signal intensity was observed. This decrease in the intensity should be assigned to the reduction of ammonia. Meanwhile, it was known that the evolution of K signal was closely related with the formation of Cu-O-Ce solution solid [65]. Thus the amount of Cu-O-Ce solution solid was lower after ammonia treatment. This phenomenon should be attributed to the reaction of the NH_x species with lattice oxygen in Cu-O-Ce solution solid through this step:



The NH₃-TPR results have demonstrated the formation of N₂ and N₂O. Though no trace of the EPR signal corresponding to Ce³⁺ was observed during NH₃-TPR, the higher Ce³⁺/Ce⁴⁺ molar ratio in comparison with the original one has been obtained (Fig. 17A and Table 2). The O1s XPS spectra of the CuO-CeO₂ catalyst during NH₃-TPR cycles are shown in Fig. 17B. The main peak was centered at a

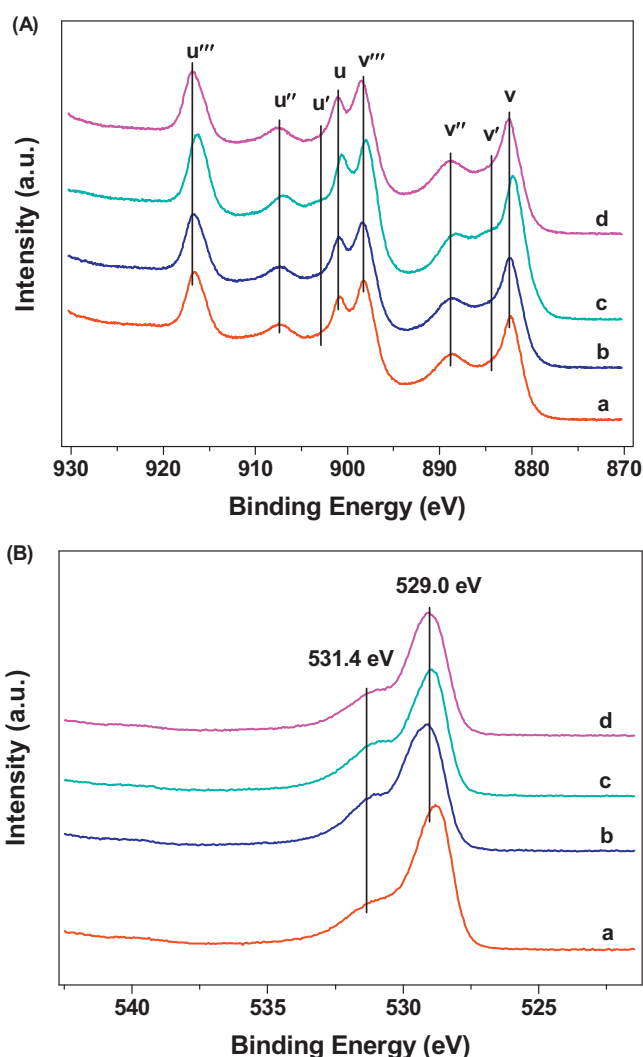
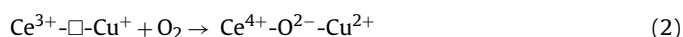


Fig. 17. XPS spectra of Ce 3d (A) and O 1s (B) for 10-CuO-CeO₂ (ST/500) catalysts after NH₃-TPR cycles: (a) initial sample; (b) the first NH₃-TPR cycle; (c) the third NH₃-TPR cycle; (d) treatment by O₂ at 200 °C followed the third NH₃-TPR cycle.

binding energy (BE) of approximately 529.0 eV, which was characteristic of lattice oxygen (O_{latt}) [34]. While the broad shoulder at a higher BE (531.4 eV) may be attributed to surface adsorbed oxygen (O_{ads}) species [66]. As listed in Table 2, the O_{latt}/O_{ads} molar ratio (1.32) significantly decreased in comparison with that of the original sample (1.69) after the first NH₃-TPR cycle. With the successive cycles, the O_{latt}/O_{ads} molar ratio was only 1.26 after the third NH₃-TPR cycle (Fig. 17B(c)). Thus, the lattice oxygen in Cu-O-Ce solution solid can be consumed by NH_x species during the reaction process as shown in Eq. (1).

The reoxidation of the previous reduced CuO-CeO₂ catalysts under an oxygen atmosphere at 200 °C progressively led to complete regeneration of the original intensity of K signal (Fig. 16(c)). This regeneration in intensity could be explained by the following equation:



It seems that the gaseous oxygen was responsible for the coupling between the two copper (II) ions making up the dimers, as described in Scheme 1. Moreover, the results of XPS have indicated the decrease of the surface Ce³⁺/Ce⁴⁺ molar ratio of CuO-CeO₂ catalyst after treatment with O₂ at 200 °C (Table 2 and Fig. 17A(d)). Simultaneously, the O_{latt}/O_{ads} molar ratio considerably increased

to 1.91. Thus, the Cu–O–Ce solid solution played an important role in the migration and activation of oxygen in the NH_3 –SCO reaction. The lattice oxygen in Cu–O–Ce solid solution can be consumed by NH_x species, and the gas-phase oxygen refilled oxygen vacancy sites to replenish lattice oxygen and maintain the oxygen circulation in NH_3 oxidation reaction, whose result was consistent with the conclusion in Section 3.4.3.

In addition, it has been observed that the intensity of O signal decreased significantly and even disappeared after CuO–CeO₂ catalyst was treated with O₂ at 200 °C (Fig. 16(c)) and reaction gas ($\text{NH}_3 + \text{O}_2$) at 200 °C or 260 °C (Fig. 16(d) or (e)). It has been known that the intensity of O signal was correlated with the dispersion of copper oxide on the surface [66], and the larger fraction oxidation of copper would make the escaped EPR detection of CuO [67]. However the H₂–TPR and XRD technologies demonstrated that the finely dispersed CuO species was still present in 10–CuO–CeO₂ (ST/500) samples treated by reaction gas ($\text{NH}_3 + \text{O}_2$) and no larger CuO particles was observed (Fig. S5). So the precise reason about the change of signal O in EPR was still not very clear, and it may be related with lower dispersion degree of finely dispersed CuO or gas oxygen, which will be investigated in the near future.

When the sample was treated with reaction gas ($\text{NH}_3 + \text{O}_2$) at 200 °C, the increase in the K signal intensity (Fig. 16(d)) compared with the original sample (Fig. 16(a)) was observed, which may be related with the quickly reversible process of Eq. (1) and Eq. (2) in NH_3 –SCO reaction. Also the higher treatment temperature (260 °C) led to the further increase of the K signal intensity (Fig. 16(e)). The increase of K signal intensity compared with the original sample (Fig. 16(a)) suggested the concentration increase of Cu–O–Ce solid solution in CuO–CeO₂ catalyst, which should be due to the intrinsic Ce^{3+} –□–Cu⁺ in CuO–CeO₂ catalyst. It has been known the presence of the Ce^{3+} and Cu⁺ in the initial CuO–CeO₂ catalyst (Fig. 4). In the presence of gaseous oxygen, the intrinsic Ce^{3+} –□–Cu⁺ could react with oxygen to form Ce^{4+} –O^{2–}–Cu²⁺ (Eq. (2)), subsequently, promote the reaction of Eq. (1). Moreover the reactions of Eq. (1) and Eq. (2) became easier in NH_3 –SCO reaction at higher temperature because the higher temperature made the oxygen activation or migration and the NH_3 adsorption/activation is more intense.

Based on the above analysis, the reaction route of NH_3 –SCO reaction on CuO–CeO₂ catalyst was depicted in Scheme 2. The finely dispersed CuO species was the main adsorbed sites for NH_3 molecules. Then the adsorbed NH_3 could be transferred on the surface of CeO₂ under the synergetic interaction between copper and ceria species, which further was activated and transformed into NH_x species by ceria in the roles of quick change of chemical state in near-surface region and the strong electron state interaction in CuO–CeO₂ catalysts. The Cu–O–Ce solid solution promoted the activation of gas oxygen and the formation and migration of lattice oxygen. When oxygen was absent, the activated intermediates (NH_x) on CeO₂ could be produced from the adsorbed NH_3 and react with the lattice oxygen to form N₂ and N₂O (Eq. (1)). Simultaneously, the more oxygen vacancies sites were produced. On the other hand, when gaseous oxygen was present, it readily refilled the formed oxygen vacant sites, and then promoted the NH_3 –SCO reaction. Additionally, the situ-formed intermediate NO on CeO₂ in the presence of gaseous oxygen could also react with $\text{NH}_{3(\text{ad})}$ to form N₂, which was selectively catalyzed by CuO. Nevertheless, the further experiments were still required in order to thoroughly study the detailed intermediates and active sites in NH_3 –SCO reaction.

4. Conclusions

In this study, the CuO–CeO₂ catalysts have been characterized and tested in NH_3 –SCO reaction. In comparison with CuO–CeO₂ (STI) and CuO–CeO₂ (CI) catalysts prepared by different methods,

CuO–CeO₂ (ST) catalysts prepared by surfactant-templated method displayed the best activity for NH_3 oxidation. Furthermore, the NH_3 conversion over the CuO–CeO₂ (ST) catalyst was, on average, 25% higher than those Cu–Ce catalysts prepared by co-precipitation in previous research under the same test conditions. It was observed that Cu loading and calcination temperature noticeably affected the crystallite size, dispersion degree of CuO species and their catalytic activity. Particularly, 10–CuO–CeO₂ (ST/500) catalyst showed the highest NH_3 conversion and the lowest complete conversion temperature of 250 °C, which was ascribed to the higher molar ratio of the finely dispersed CuO species, the smaller particle size of CeO₂ and strong synergetic interaction between copper oxide species and ceria oxides. This synergetic interaction between the two components, quick change of chemical state in near-surface region and the strong electron state interaction greatly enhanced the adsorption and activation of NH_3 molecules. The activation of ammonia by ceria led to the formation of N₂ and NO_x, followed by the oxidation between NO and $\text{NH}_{3(\text{ad})}$ selectively catalyzed by CuO to N₂. In addition, the lattice oxygen provided by Cu–O–Ce solid solution in CuO–CeO₂ (ST) catalyst could also react with the activated intermediates (NH_x) to produce N₂ and N₂O. When the lattice oxygen was completely consumed, the gas oxygen could refill the oxygen vacancies in Cu–O–Ce solid solution to maintain $\text{Ce}^{4+}/\text{Ce}^{3+}$ redox couple. The presence of the Cu–O–Ce solid solution promoted the activation of gas oxygen and the formation and migration of lattice oxygen in NH_3 –SCO reaction.

Acknowledgements

This work was supported by the National High Technology Research and Development Program of China (863 Program) (No. 2009AA062604), the Program for New Century Excellent Talents in University (NCET-09-0256) and the Program for Changjiang Scholars and Innovative Research Team in University (IRT0813).

Appendix A. Supplementary data

Supplementary data associated with this article can be found, in the online version, at <http://dx.doi.org/10.1016/j.apcatb.2013.01.029>.

References

- [1] H.M.J. Kušar, A.G. Ersson, M. Vosecký, S.G. Järås, *Applied Catalysis B: Environmental* 58 (2005) 25–32.
- [2] Y.J. Li, J.N. Armor, *Applied Catalysis B: Environmental* 13 (1997) 131–139.
- [3] Z. Wang, Z.P. Qu, X. Quan, H. Wang, *Applied Catalysis A: General* 411–412 (2012) 131–138.
- [4] L. Chmielarz, P. Kuśtrowski, A.R. Lasocha, R. Dziembaj, *Applied Catalysis B: Environmental* 58 (2005) 235–244.
- [5] M. Amblard, R. Burch, B.W.L. Southward, *Applied Catalysis B: Environmental* 22 (1999) 159–166.
- [6] S.L. He, C.B. Zhang, M. Yang, Y. Zhang, W.Q. Xu, N. Cao, H. He, *Separation and Purification Technology* 58 (2007) 173–178.
- [7] G. Lu, J. van Grondelle, B.G. Anderson, R.A. van Santen, *Journal of Catalysis* 186 (1999) 100–109.
- [8] R.Q. Long, R.T. Yang, *Journal of Catalysis* 207 (2002) 158–165.
- [9] N.N. Sazonova, A.V. Simakov, T.A. Nikoro, G.B. Barannik, V.F. Lyakhova, V.I. Zheivot, Z.R. Ismagilov, H. Veringa, *Catalysis Letters* 57 (1996) 71–79.
- [10] C.M. Hung, *Powder Technology* 196 (2009) 56–61.
- [11] P. Bazin, O. Saur, O. Marie, M. Daturi, J.C. Lavalley, A.M. Le Govic, V. Harlé, G. Blanchard, *Applied Catalysis B: Environmental* 119–120 (2012) 207–216.
- [12] S. Scire, C. Crisafulli, P.M. Riccobene, G. Patanè, A. Pistone, *Applied Catalysis A: General* 417–418 (2012) 66–75.
- [13] P.O. Larsson, A. Andersson, *Applied Catalysis B: Environmental* 24 (2000) 175–192.
- [14] W. Liu, M. Flytzanistephanopoulos, *Journal of Catalysis* 153 (1995) 304–316.
- [15] J.A. Rodriguez, P. Liu, J. Hrbek, J. Evans, M. Pérez, *Angewandte Chemie International Edition* 119 (2007) 1351–1354.
- [16] G. Avgouropoulos, T. Ioannides, H. Matralis, *Applied Catalysis B: Environmental* 56 (2005) 87–93.
- [17] J.R. Kim, W.J. Myeong, S.K. Ihm, *Journal of Catalysis* 263 (2009) 123–133.

- [18] J. Papavasiliou, G. Avgouropoulos, T. Ioannides, *Applied Catalysis B: Environmental* 66 (2006) 168–174.
- [19] D.A. Constantinou, A.M. Efstathiou, *Applied Catalysis B: Environmental* 96 (2010) 276–289.
- [20] C.R. Jung, A. Kundu, S.W. Nam, H.I. Lee, *Applied Catalysis B: Environmental* 84 (2008) 426–432.
- [21] J.C. Lou, C.M. Hung, S.F. Yang, *Journal of the Air & Waste Management Association* 54 (2004) 68–76.
- [22] C.V. Ovesen, P. Stoltze, J.K. Nørskov, C.T. Campbell, *Journal of Catalysis* 134 (1992) 445–468.
- [23] F. Marino, C. Descorme, D. Duprez, *Applied Catalysis B: Environmental* 58 (2005) 175–183.
- [24] M. Manzoli, R.D. Monte, F. Boccuzzi, S. Coluccia, J. Kašpar, *Applied Catalysis B: Environmental* 61 (2005) 192–205.
- [25] J.A. Rodriguez, S. Ma, P. Liu, J. Hrbek, J. Evans, M. Pérez, *Science* 318 (2007) 1757–1760.
- [26] M. Turco, C. Cammarano, G. Bagnasco, E. Moretti, L. Storaro, A. Talon, M. Lenarda, *Applied Catalysis B: Environmental* 91 (2009) 101–107.
- [27] W.H. Shen, X.P. Dong, Y.F. Zhu, H.R. Chen, J.L. Shi, *Microporous and Mesoporous Materials* 85 (2005) 157–162.
- [28] I. Atribak, B. Azambre, A.B. López, A. García-García, *Applied Catalysis B: Environmental* 92 (2009) 126–137.
- [29] P. Bera, K.R. Priolkar, P.R. Sarode, M.S. Hegde, S. Emura, R. Kumashiro, N.P. Lalla, *Chemistry of Materials* 14 (2002) 3591–3601.
- [30] J. Fan, X.D. Wu, X.D. Wu, Q. Liang, R. Ran, D. Weng, *Applied Catalysis B: Environmental* 81 (2008) 38–48.
- [31] A. Galdikas, C. Descorme, D. Duprez, F. Dong, H. Shinjoh, *Topics in Catalysis* 30/31 (2004) 405–409.
- [32] J. Li, Y.X. Han, Y.H. Zhu, R.X. Zhou, *Applied Catalysis B: Environmental* 108–109 (2011) 72–80.
- [33] W.J. Shan, Z.C. Feng, Z.L. Li, J. Zhang, W.J. Shen, C. Li, *Journal of Catalysis* 228 (2004) 206–217.
- [34] G. Avgouropoulos, T. Ioannides, *Applied Catalysis B: Environmental* 67 (2006) 1–11.
- [35] L.J. Kundakovic, M.F. Stephanopoulos, *Applied Catalysis A: General* 171 (1998) 13–29.
- [36] L. Qi, Q. Yu, Y. Dai, C.J. Tang, L.J. Liu, H.L. Zhang, F. Gao, L. Dong, Y. Chen, *Applied Catalysis B: Environmental* 119–120 (2012) 308–320.
- [37] H. Vidal, J. Kašpar, M. Pijolat, G. Colon, S. Bernal, A. Cordón, V. Perrichon, F. Fally, *Applied Catalysis B: Environmental* 27 (2000) 49–63.
- [38] M.F. Luo, J.M. Ma, J.Q. Lu, Y.P. Song, Y.J. Wang, *Journal of Catalysis* 246 (2007) 52–59.
- [39] E.M. Slavinskaya, S.A. Veniaminov, P. Notté, A.S. Ivanova, A.I. Boronin, Yu.A. Chesalov, I.A. Polukhina, A.S. Noskov, *Journal of Catalysis* 222 (2004) 129–142.
- [40] J. Wang, T. Yu, X.Q. Wang, G.S. Qi, J.J. Xue, M.Q. Shen, W. Li, *Applied Catalysis B: Environmental* 172 (2012) 137–147.
- [41] M.Y. Kustova, S.B. Rasmussen, A.L. Kustov, C.H. Christensen, *Applied Catalysis B: Environmental* 67 (2006) 60–67.
- [42] A.A. Kaïs, A. Bennani, C.F. Aïssi, M. Guelton, J.C. Vedrine, *Chemistry of Materials* 4 (1992) 977–979.
- [43] G.R. Rao, H.R. Sahu, B.G. Mishra, *Colloids and Surfaces A: Physicochemical and Engineering Aspects* 220 (2003) 261–269.
- [44] C.B. Azzoni, A. Paleari, G.B. Parravicini, *Journal of Physics: Condensed Matter* 4 (1992) 1359–1366.
- [45] A.A. Kaïs, A. Bennani, C.F. Aïssi, G. Wrobel, M. Guelton, *Journal of the Chemical Society, Faraday Transactions* 88 (1992) 615–622.
- [46] M.F. Ribeiro, J.M. Silva, S. Brimaud, A.P. Antunes, E.R. Silva, A. Fernandes, P. Magnoux, D.M. Murphy, *Applied Catalysis B: Environmental* 70 (2007) 384–392.
- [47] S.S. Eaton, K.M. More, B.M. Sawant, G.R. Eaton, *Journal of the American Chemical Society* 105 (1983) 6560–6567.
- [48] S.S. Eaton, G.R. Eaton, C.K. Chang, *Journal of the American Chemical Society* 107 (1985) 3177–3184.
- [49] M.F. Luo, Y.J. Zhong, X.X. Yuan, X.M. Zheng, *Applied Catalysis A: General* 162 (1997) 121–131.
- [50] B. Bahrami, V.G. Komvokis, M.S. Ziebarth, O.S. Alexeev, M.D. Amiridis, *Applied Catalysis B: Environmental* 130–131 (2013) 25–35.
- [51] G. Ramis, L. Yi, G. Busca, M. Turco, E. Kötur, R.J. Willey, *Journal of Catalysis* 157 (1995) 523–535.
- [52] M. Adamowska, S. Muller, P.D. Costa, A. Krzton, P. Burg, *Applied Catalysis B: Environmental* 74 (2007) 278–289.
- [53] X.Z. Cui, J. Zhou, Z.Q. Ye, H.R. Chen, L. Li, M.L. Ruan, J.L. Shi, *Journal of Catalysis* 270 (2010) 310–317.
- [54] S. Hong, A. Karim, T.S. Rahman, K. Jacobi, G. Ertl, *Journal of Catalysis* 276 (2010) 371–381.
- [55] J.J. Luo, H.Y. Xu, Y.F. Liu, W. Chu, C.F. Jiang, X.S. Zhao, *Applied Catalysis A: General* 423–424 (2012) 121–129.
- [56] D. Delimaris, T. Ioannides, *Applied Catalysis B: Environmental* 89 (2009) 295–302.
- [57] Z. Zhu, Z. Liu, S. Lin, H. Niu, T. Hu, T. Liu, *Applied Catalysis B: Environmental* 26 (2000) 25–35.
- [58] J.F. Chen, Y.Y. Zhan, J.J. Zhu, C.Q. Chen, X.Y. Lin, Q. Zheng, *Applied Catalysis A: General* 377 (2010) 121–127.
- [59] C.M. Hung, *Journal of Hazardous Materials* 166 (2009) 1314–1320.
- [60] Y. Hu, L. Dong, M. Shen, D. Liu, J. Wang, W. Ding, Y. Chen, *Applied Catalysis B: Environmental* 31 (2001) 61–69.
- [61] V.A. Kondratenko, M. Baerns, *Applied Catalysis B: Environmental* 70 (2007) 111–118.
- [62] J.M.G. Amores, V.S. Escibano, G. Ramis, G. Busca, *Applied Catalysis B: Environmental* 13 (1997) 45–58.
- [63] L. Gang, B.G. Anderson, J. van Grondelle, R.A. van Santen, *Journal of Catalysis* 199 (2001) 107–114.
- [64] M.V. Bukhtiyarova, A.S. Ivanova, E.M. Slavinskaya, L.M. Plyasova, V.V. Kaichev, P.A. Kuznetsov, *Applied Catalysis A: General* 384 (2010) 230–240.
- [65] J. Sofia, J.C. Conesa, A. Martinez-Arias, J.M. Coronado, *Solid State Ionics* 63–65 (1993) 755–761.
- [66] Y.S. Xia, H.X. Dai, L. Zhang, J.G. Deng, H. He, C.T. Au, *Applied Catalysis B: Environmental* 100 (2010) 229–237.
- [67] R. Cousin, S. Capelle, E. Abi-Aad, D. Courcot, A. Aboukaïs, *Chemistry of Materials* 13 (2001) 3862–3870.